Ocean–wave coupled modeling in COAMPS-TC: A study of Hurricane Ivan (2004)

Travis A. Smith [a,*], Sue Chen [b], Timothy Campbell [a], Paul Martin [a], W. Erick Rogers [a], Saša Gaberšek [b], David Wang [a], Suzanne Carroll [c], Richard Allard [a]

[a] Naval Research Laboratory, Stennis Space Center, MS 39529, United States
[b] Naval Research Laboratory, 7 Grace Hopper Ave., Monterey, CA 93943, United States
[c] QinetiQ North America, Stennis Space Center, MS 39529, United States

ARTICLE INFO

ABSTRACT

Tropical cyclone ocean–wave model interactions are examined using an ESMF – (Earth System Modeling Framework) based tropical cyclone (TC) version of the Coupled Ocean/Atmosphere Mesoscale Prediction System (COAMPS®1). This study investigates Hurricane Ivan, which traversed the Gulf of Mexico (GOM) in September 2004. Several oceanic and wave observational data sets, including Acoustic Doppler Current Profilers (ADCPs), National Oceanic and Atmospheric Administration (NOAA) buoys, satellite altimeter data, and Scanning Radar Altimeter (SRA) data, allow for a unique analysis of the coupled atmosphere, ocean (Navy Coastal Ocean Model, NCOM), and wave (Simulating WAves Nearshore, SWAN) models in COAMPS-TC. To determine the feasibility of coupling NCOM to SWAN in high-wind conditions during Hurricane Ivan, near-surface currents in NCOM were first compared to near-surface ADCP observations. Recent modifications to SWAN, including new wind-to-wave energy input and wave-breaking energy dissipation source functions, as well as a new ocean surface drag coefficient formulation appropriate for high-wind conditions, significantly improved the forecast wave field properties, such as significant wave height (SWH), in TC conditions. Further results show that the ocean-to-wave model coupling, which allows for the strong, hurricane-induced, surface currents in NCOM to interact with SWAN, provided additional improvements to the forecast SWH field. Additionally, wave-to-ocean model coupling, which included the input of the Stokes Drift Current (SDC) calculated from the SWAN wave spectra to NCOM, is examined. The models indicate that the SDC was on the order of 10–25% of the near-surface Eulerian current during Ivan. Recent studies of the importance of the SDC and the resulting Langmuir turbulence on vertical ocean mixing in TCs is also discussed.

Published by Elsevier Ltd.

1. Introduction

Air–sea interaction has long been recognized as an essential factor in the numerical prediction of many atmospheric and oceanic phenomena, including tropical cyclones (TCs). The coupling of state-of-the-art atmosphere, ocean, and wave models allows for a more precise representation of the complicated physical processes occurring near the air-sea interface. Fully air-ocean-wave coupled modeling has only come to fruition recently. However, model coupling, whether it is air-wave, air-ocean, or ocean-wave coupling, has long been studied in research and operational environments. For example, numerous European Centre for Medium-Range Forecasts (ECMWF) studies by Peter Janssen and collaborators (e.g., Janssen and Viterbo, 1996; Janssen et al., 2000, 2002) present a global diagnosis of ocean–wave forecasting, including the effects of ocean waves on the atmospheric climate. Additionally, three-dimensional, air–ocean–wave coupled model advancements in the coastal zone have led to a significant increase in understanding sediment transport, even in TC conditions (Warner et al., 2008, 2010).

The advancement of fully-coupled, air–ocean–wave modeling has traditionally been hindered by uncertainty in the parameterization of air–sea interactions and the technical difficulty of coupling complex modeling systems. However, recent improvements in the parameterizations and computational techniques used in the Earth System Modeling Framework (ESMF) have allowed for high-resolution application of fully-coupled, air–ocean–wave models. This particular study utilizes an ESMF-based coupled system, the Coupled Ocean Atmosphere Mesoscale Prediction System-Tropical Cyclone (COAMPS-TC), in which all the interactions between the atmosphere, ocean, and wave models occur within an ESMF driver that exchanges information between the three models.

* Corresponding author. Tel.: +1 228 688 5631; fax: +1 228 688 4759.
E-mail address: travis.smith@nrlssc.navy.mil (T.A. Smith).
1 COAMPS® is a registered trademark of the Naval Research Laboratory.

A prime example of an extreme case of air–sea interaction occurs with the passage of a TC. Heat and momentum fluxes, wind stresses, and complex wave–current interactions play a pivotal role in both the intensity and structure of TCs. There have been many theoretical and numerical modeling studies of the ocean response to TCs. TC-induced effects on the ocean include SST cooling, strong surface currents (which can exceed 2 m s^{-1}), upwelling and down-welling, large-amplitude surface waves, and large internal gravity waves (Price, 1981; Ginis et al., 1989; Jacob et al., 2000; Morey et al., 2006; Fan et al., 2009a,b). The atmospheric response of TCs to the SST and upper-ocean heat content is well documented (Knaff et. al., 2013 and references cited within); however, the atmospheric response to wave momentum and moisture flux exchange (e.g., sea spray) is a current focus of study in air–sea coupled modeling. These wind–wave–current interactions and coupled processes in TCs are not well understood and efforts are currently ongoing to improve both the understanding and numerical modeling of them (Drennan et al., 2003; Hara and Belcher, 2004; Moon et al., 2004a,b; Chen et al., 2010; Donelan et al., 2012).

One of the primary limiting factors in studies involving wind–wave–current interactions during TCs is insufficient in situ data. Although open-ocean, tropical cyclone wind and pressure measurements are frequently sampled using radiosondes, in situ current and wave measurements in hurricane conditions have been sparse and lack sufficient spatial and temporal resolution to investigate the ocean response in detail (Shay et al., 1989). Difficulties in forecasting both the initiation and track of TCs have led researchers to rely on chance encounters by ocean buoys, moorings, and instruments that have usually been deployed for other purposes.

The Acoustic Doppler Current Profiler (ADCP) array utilized in this study (Fig. 1) was part of the Naval Research Laboratory's (NRL's) Slope to Shelf Energetics and Exchange Dynamics (SEED) project, an intensive measurement program of the outer continental shelf and upper-slope waters of the northern Gulf of Mexico (GOM) (Mitchell et al. 2005; Wang et al. 2005; Teague et al. 2006). In September 2004, Hurricane Ivan, with maximum sustained winds greater than 50 m s^{-1}, passed directly over the SEED array. All the moorings survived to provide one of the best data sets of ocean current profile measurements ever obtained in such extreme conditions. Historically, instruments that experience a chance encounter with a major TC usually fail before the most intense conditions are measured. For example, the National Oceanic and Atmospheric Administration (NOAA) National Weather Service National Data Buoy Center (NDBC) buoy 42040 was directly impacted by the inner core of Hurricane Ivan and failed shortly thereafter. This particular buoy measured record significant wave heights in excess of 15 m before the buoy stopped reporting, readings that have since been verified as accurate.

The in situ data sets were also complemented by observations from reconnaissance aircraft that flew special missions into Hurricane Ivan as the storm traversed the Caribbean Sea and southern GOM. These flights measured high-resolution wave spectra and sea-surface topography from Scanning Radar Altimeter (SRA) observations through a joint effort between the National Aeronautics and Space Administration (NASA) Goddard Space Flight Center and the NOAA/Atlantic Oceanographic and Meteorological Laboratory/Hurricane Research Division (HRD). Additionally, several satellite altimeter passes (e.g., the European Remote Sensing Satellite, ERS-2) also provided useful wind-wave information for the period of interest. The combination of all these observational datasets allows for a unique analysis of the hurricane's wind–wave–current interaction.

This study utilizes NRL's COAMPS-TC (Doyle et al., 2012) for tropical cyclone modeling, while focusing on the ocean–wave model interactions during the high-wind TC conditions of Hurricane Ivan as it traversed the GOM. COAMPS-TC employs the state-of-the-art ESMF to exchange wind, wave, and current information across the air–sea interface (Campbell et al., 2010). New Simulating Waves Nearshore (SWAN) wind-to-wave energy input and wave-breaking energy dissipation source functions (Donelan et al., 2006; Babanin et al., 2010; Rogers et al., 2012) based on observational studies (Young et al., 2005; Donelan et al., 2006;
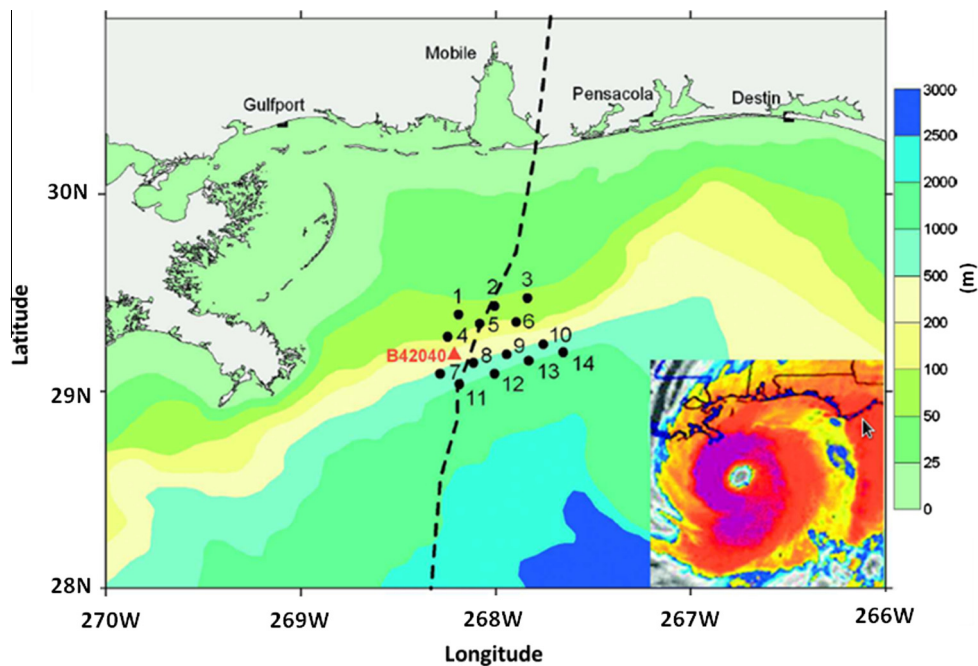

Fig. 1. Location of the ADCP array in the northern GOM during September 2004 (Teague et al., 2007). Bathymetry (color contours), the location of NDBC buoy 42040 (red triangle), and the best track from the observations of Hurricane Ivan (hatched line) are shown. Inset: Infrared satellite picture (red hues indicate higher and colder cloud tops) of Hurricane Ivan as the TC approached the northern GOM coast on 15 September 2004.

Babanin et al., 2007) are tested in TC conditions, as well as a new formulation of the SWAN ocean surface drag coefficient derived from high wind observations (Hwang, 2011). Additionally, ocean-to-wave model coupling, which includes the input of the Navy Coastal Ocean Model (NCOM) ocean surface currents and water levels to SWAN, is explored through observational comparisons of both coupled and uncoupled ocean–wave model interaction simulations for Hurricane Ivan. Finally, wave-to-ocean model coupling is examined through the Stokes Drift Current (SDC) generated by the surface waves predicted by SWAN. New idealized studies (e.g., Van Roekel et al., 2012) show that the angle between the surface atmospheric wind stress and the SDC is important in the generation of Langmuir turbulence (LT) and mixing in the upper ocean. A misalignment angle greater than zero tends to decrease LT and a misalignment angle greater than 90° tends to inhibit LT and mixing. In extreme situations such as TCs, the misalignment angle between the SDC and the wind stress can commonly exceed 90°, depending on the direction of the swell and the translation direction of the TC (Sullivan et al., 2012). The relationship between the SDC and the surface wind stress is examined for Hurricane Ivan near the eyewall, where surface wind direction changes occur rapidly over short distances.

Section 2 is a general discussion of air-ocean-wave coupling parameters in COAMPS-TC. Section 3 discusses the COAMPS-TC model setup for Hurricane Ivan and describes the in situ data. Section 4 presents an evaluation of the near-surface currents from the Hurricane Ivan simulation based on the ADCP measurements. The results of utilizing the new SWAN wind input and drag coefficient parameterizations and the NCOM/SWAN coupling are also presented in Section 4. Section 5 provides a summary and a discussion of future coupling applications with COAMPS-TC.

2. Air–ocean–wave coupling methods in COAMPS-TC

A fully-coupled, air–ocean–wave model can provide frequent, two-way feedback between the air, ocean, and wave components. In COAMPS-TC, the atmospheric component provides surface atmospheric pressure and momentum, heat, and moisture fluxes to the ocean component, while the ocean model returns its predicted SST to the atmosphere, which influences the prediction of the atmospheric model, including the surface air–sea fluxes, on its next time step (Chen et al., 2010).

The feedback of the wave model to the atmosphere consists of a non-dimensional roughness length (Charnock number), which is used to compute the atmospheric momentum drag. Either of two different empirical formulations for the Charnock number (Doyle, 2002; Moon et al., 2004a,b), which are a function of wave age and wind speed, can be selected. For this study, we employed the wind–wave coupling from Moon et al. (2004b). Although not a focus of this study, the ocean–atmosphere and wave–atmosphere coupling are important to the intensity of the TC.

The feedback of the ocean component to the wave component includes the input of NCOM surface currents and water levels to SWAN, while the atmospheric component impacts the wave field though the input of the TC winds. Water levels can modify the water depth utilized within the wave model physics calculations, though this effect is only significant if the water depth is sufficiently shallow that the waves feel the bottom. More importantly, the surface currents input to the wave model alter the effective wind speed (i.e., the wind speed relative to a frame of reference moving with the currents) and the horizontal shear of the currents produces changes in the length, height, and direction of the waves in a manner similar to refraction and shoaling by interaction with variable bathymetry. These are conservative processes; e.g., shoaling is associated with conservation of the wave energy flux. However, this can, in turn, lead to non-conservative effects. For

example, waves that become more (or less) steep due to interaction with currents will be more (or less) likely to break, and this breaking, also called whitecapping, is a highly nonlinear and non-conservative process. The effect of whitecapping is discussed later in Section 4, which shows results for Hurricane Ivan with and without ocean-to-wave coupling and comparison to in situ observational data.

The feedback of the wave component to the ocean component (i.e., SWAN to NCOM) includes the SDC, the wave radiation stress gradients, and the characteristic velocity and frequency of the wave orbital motion near the bottom. The wave motion near the bottom is used to enhance the bottom drag in shallow water using the parameterization described by Signell et al. (1990) and Davies and Lawrence (1994). The wave-radiation stress gradients from SWAN are applied in NCOM as a surface stress. The SDC from SWAN is included within the Coriolis term in NCOM's momentum equations (this is referred to as the Stokes–Coriolis term), is used to advect all the ocean model fields, and is included within NCOM's continuity equation (these SDC terms are implemented as in Bennis et al., 2011). The SDC is also used in the parameterization of the enhancement of vertical mixing by LT as described by Kantha and Clayson (2004), i.e., additional shear-production terms, which consist of the product of the vertical shear of the SDC and the vertical turbulent momentum flux (which are referred to as Stokes production terms), are added to the turbulent kinetic energy (TKE) and vertical turbulent length-scale (TLS) equations in the Mellor–Yamada Level 2.5 (MYL2.5) turbulence model used to compute the vertical mixing coefficients in NCOM (see Appendix B).

The primary focus of the wave-to-ocean coupling in this study is on the effects of the SDC in TC conditions. Although the physical effects of the SDC had not been thoroughly studied until recently, early studies assumed the SDC to be primarily aligned with the surface wind stress. However, Hanley et al. (2010) found that seas are rarely in wind-wave equilibrium and always produce some misalignment between the wind and the waves. In particular, propagating swell waves are susceptible to misalignment with the wind direction (Hanley et al., 2011). Van Roekel et al. (2012) show in their idealized large-eddy simulation (LES) studies that a greater misalignment angle between the wind and the waves decreases the generation of LT and that, in extreme cases, when the SDC directly opposes the wind stress, there may be minimal generation of LT and an associated decrease in upper-ocean mixing. In terms of the sheer structure of a TC, large wind waves and swell combined with quick changes in the wind direction associated with the eye, or inner core, of the TC may produce a large misalignment angle between the wind stress and the SDC. The numerical modeling studies of Sullivan et al. (2012), which included LES of LT, indicate that misalignment between the wind and waves near the eye of a hurricane can result in reduced mixing. In the simulations of Hurricane Ivan conducted here, the effect of misalignment of the wind and waves on LT and, consequently, vertical mixing is parameterized by the Stokes TKE production terms in the MYL2.5 turbulence model (Kantha and Clayson, 2004) as discussed in Appendix B. Calculations of the COAMPS-TC SDC and subsequent TKE generation associated with the SDC are presented in Section 4.

3. COAMPS-TC model configuration and observational data

3.1. Model setup

The coupled COAMPS-TC system consists of two independent, three-dimensional, variational (3DVAR) atmosphere and ocean data assimilation systems, three forecast models (atmosphere, ocean, and wave), and a coupler that functions as a router to distribute the model forecast fields between each pair of forecast

components. Details of the model operation and the associated air–ocean exchanges are discussed in Chen et al. (2010). The atmospheric data assimilation is a special version of the Navy Atmospheric Variational Data Assimilation System (NAVDAS, Daley and Barker, 2001) that includes TC relocation and initialization algorithms. At the analysis time, the first-guess fields are relocated to the observed TC location. Next, the new first-guess fields are combined with 49 synthetic atmospheric temperature, moisture, and wind profiles at nine vertical levels to better define the TC and its immediate environment. In addition, NAVDAS uses a reduced correlation length scale and relaxation of the geostrophic balance near the TC center to improve the covariance used in the analysis (Liou and Sashegyi, 2011). For NCOM, the Navy Coupled Ocean Data Assimilation (NCODA) 3DVAR system is an equivalent oceanographic implementation of NAVDAS (Cummings, 2005; Smith et al., 2011). In two-dimensional mode, NCODA analyzes the SST, sea ice, significant wave height (SWH), and sea-surface height (SSH) using a univariate assimilation method. The three-dimensional (3D) analysis of sea temperature, salinity, and u (east/west) and v (north/south) currents is multivariate. NCODA has options to perform assimilation on either the native ocean model vertical grid or on constant-depth levels. When the COAMPS-TC system is run in cycling mode, the NAVDAS and NCODA data assimilations are run sequentially at the beginning of every 12-h analysis/forecast cycle.

The COAMPS-TC model setup for Hurricane Ivan (Fig. 2) consists of a triple-nested atmospheric domain with 18-, 6-, and 2-km horizontal resolution and a total of 60 terrain-following vertical levels. The outer nest extends from the equator to 38° N and from 65° W to 108° W, with horizontal dimensions of 250 × 250. The two inner nests translate in tandem with the cyclone's vortex center. Atmospheric boundary conditions are provided by the Navy Global Atmospheric Prediction System (NOGAPS) model (Rosmond et al., 2002). The TC vortex initialization in NAVDAS is enabled through a TC warning message that includes location, wind radii (distance of a certain wind speed threshold from the center of circulation),

and intensity information provided by the National Hurricane Center in Miami, FL and the Joint Typhoon Warning Center in Hawaii. Each data-assimilation cycle is initiated using the prior 12-h forecast as background, incorporating quality-controlled observations from radiosondes, aircraft, satellites, ships, and surface stations.

The NCOM configuration (Fig. 2) consists of one 4-km resolution nest that encompasses the GOM and the Caribbean Sea. This ocean grid extends from 10° N to 31° N and from 67° W to 98° W, with horizontal dimensions of 800 × 600. A total of 50 vertical levels are used, with 36 sigma layers between the surface and 190-m depth (which are bottom-following in water shallower than 190 m), and 14 fixed-depth layers between 190 m and the maximum depth of 5500 m. Bathymetry is from the Navy's two-minute-resolution Digital Bathymetric Data Base (DBDB2). Initial and boundary conditions for NCOM are from a global version of NCOM (Barron et al., 2004) that was being run operationally at the Naval Oceanographic Office at Stennis Space Center, MS at this time. The NCODA 3DVAR ingests observational and global ocean data, including quality-controlled satellite, ship, profiler, and Modular Ocean Data Assimilation System (MODAS) synthetic profile data (Carnes et al., 1996) for each update cycle. The ocean model includes tides and river inflows.

The SWAN model configuration consists of one 8-km resolution nest, with horizontal dimensions of 400 × 300, that encompasses the same region as NCOM. The bathymetry used for SWAN is also from DBDB2. SWAN is run with 36 discrete directions and 25 frequency bands to resolve the wave spectra. The boundary conditions for SWAN would normally consist of energy spectra from a larger, global model, such as WAVEWATCH III (WW3). However, since the TC generates the dominant wave contributions to the wave field and the GOM is a semi-enclosed sea, boundary conditions for SWAN were not prescribed in these simulations.

The TC intensity is sensitive to ocean and wave model feedback to the atmosphere (Chen et al., 2010; Halliwell et al., 2011). In this study, the interactions between NCOM and SWAN were explored through both coupled and uncoupled ocean-wave simulations, while the ocean- and wave-model feedback to the atmosphere, as discussed in Section 2, was retained in both cases.

Hurricane Ivan was a large and intense TC in the central and eastern GOM from 0000 UTC 14 September until landfall at approximately 0700 UTC 16 September 2004. Spin-up of COAMPS-TC with 12-h atmosphere and ocean data assimilation cycles commenced at 0000 UTC 1 September. Hurricane Ivan's vortex was initialized on 0000 UTC 10 September when the well-developed cyclone was located over the Caribbean Sea. This provided a good initial ocean and wave state as Ivan entered the GOM on 14 September. For both the coupled and uncoupled model simulations, a 72-h forecast of Hurricane Ivan was generated at 0000 UTC and 1200 UTC 14 September to provide comparison with the in situ ocean and wave observational data.

3.2. Observational data description

Observational data from the GOM were supplied by a total of fourteen ADCPs (six of which were utilized in this study), five NDBC buoys, one SRA flight track, and eight satellite altimeter passes. The combination of these datasets provided a comprehensive spatial and temporal sampling of Ivan as it traversed the GOM.

The ADCPs were deployed in May 2004 along the outer continental shelf and slope in the northeastern GOM (Fig. 1). The six moorings used in this study were deployed along the shallow outer shelf in two rows of three, each with a horizontal spacing of 15 km. The first row of moorings, denoted as M1–M3, was at a depth of 60 m, while the second row, M4–M6, was at a depth of 90 m. They were deployed in Trawl Resistant Bottom Mounts (TRBMs), which
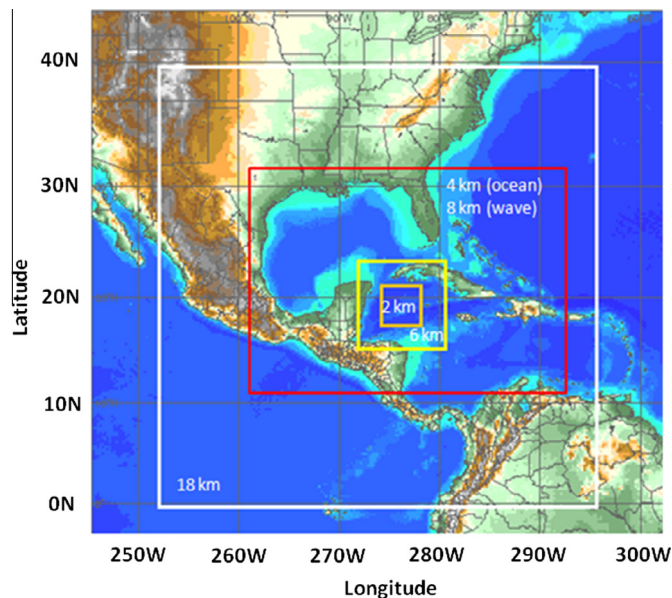

Fig. 2. Atmospheric 18-km (white), 6-km (yellow), and 2-km (orange) resolution grids and ocean/wave 4/8-km (red) resolution grids used for Hurricane Ivan simulations. The two inner atmospheric grids move in tandem with the center of the TC. The domain of the ocean and wave grids is large to allow for appropriate numerical spin-up of the cyclone over the Caribbean Sea before entering the Gulf of Mexico.

utilize dome-shaped pods known as "Barny" mounts for their barnacle-like shape (Perkins et al., 2000). The moorings were equipped with Sea-Bird Electronics wave/tide gauges and RD Instruments Workhorse ADCPs, which operated at 300 kHz. The ADCP heads were situated about 0.5 m off the sea floor and recorded current profiles with 2-m vertical resolution with an accuracy of 0.5% ± 0.5 cm s^{-1} at 15-min intervals.

Several NDBC buoys were in close proximity to Hurricane Ivan as it crossed the central and northern GOM (Fig. 3). Buoy measurements included atmospheric pressure, wind speed and direction, air and water temperature, wave energy spectra, ocean current velocity, SWH, and wave period and direction. Based on NDBC field studies, SWH accuracies are within 0.2 m or 5%, wave periods are within 1 s, and wave directions are within 10°.

The European Space Agency's GlobWave project consolidates ocean surface wind and wave data from multiple satellite instruments. This dataset is quality controlled and available through a single website for easy access. Detailed information can be found in Snaith et al. (2010). The GlobWave altimeter data for the SWAN model validation during 14–16 September 2004 were acquired from three satellites, the European Remote Sensing satellite (ERS-2), Envisat, and the GEOSAT Follow-On (GFO). These satellite altimeters provided several snapshots of the spatial variations of Ivan's wind and wave fields along its track over the GOM. Gridded model wind and wave data within 30 min of the satellite passing times were spatially interpolated to positions along the satellite tracks. Additionally, NASA reconnaissance aircraft used a SRA to collect high-resolution wave spectra and SSH data for several periods during Hurricane Ivan's lifecycle. The wave spectra from the SRA flight in the southern GOM were used to quantify the performance of

SWAN in extreme wind and wave conditions within all four quadrants of the cyclone.

4. Results

4.1. Ocean-to-wave coupling in COAMPS-TC

Low errors in the forecast track and intensity of Hurricane Ivan allowed acceptable statistical comparisons to be generated for evaluating the ocean-wave coupling in COAMPS-TC. Both NCOM-to-SWAN coupled and uncoupled COAMPS-TC simulations (details in Section 4.1.2) produced wind speed errors that were generally 5 m s^{-1} or less, with best-track errors of less than 20 nautical miles (37 km) for most of the forecast track. However, the track errors increased just before landfall along the northern GOM coast (Fig. 3). The forecast track was nearly identical for all the simulations of Hurricane Ivan as the cyclone traversed the GOM for both the 0000 UTC and 1200 UTC 14 September 2004 forecasts, which allowed for direct comparisons between the coupled and uncoupled model simulations.

4.1.1. Near-surface current response for Hurricane Ivan in COAMPS-TC

Validation of the near-surface currents in NCOM in such extreme wind conditions is quite rare, but necessary in order to evaluate the ocean-to-wave coupling performance of NCOM and SWAN. NCOM was allowed to spin up with NCODA ocean data assimilation for several weeks prior to the arrival of Hurricane Ivan in the GOM to allow pertinent ocean circulation and surface features to develop, thus providing a good initial state for the cyclone's passage across the GOM. As stated previously, the 1200
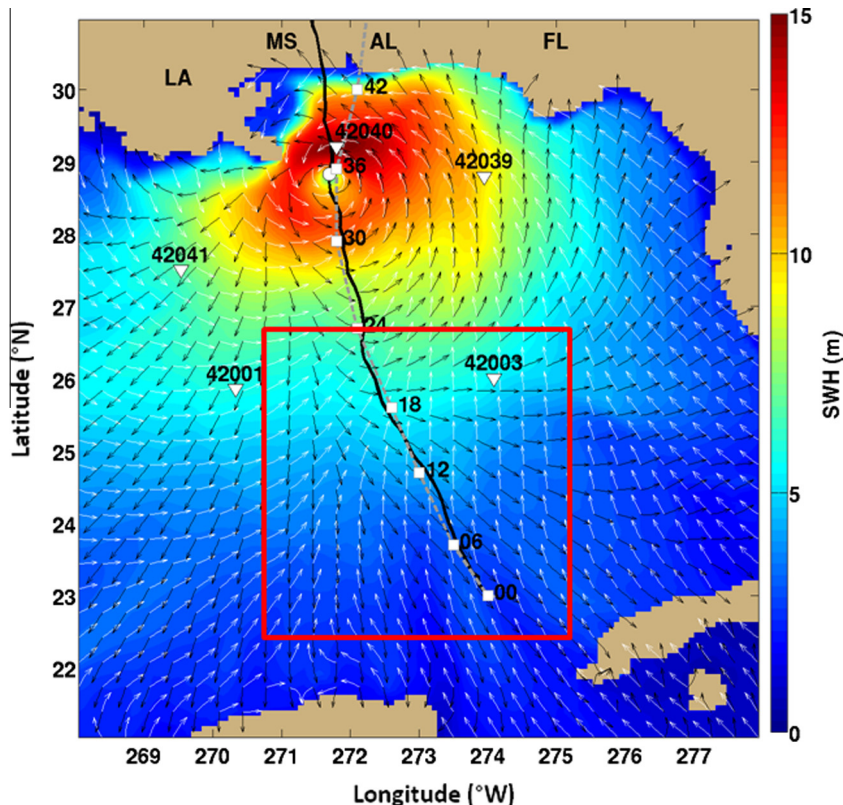

Fig. 3. The locations of NDBC buoys 42001, 42003, 42039, 42040, and 42041 are denoted by white triangles. Hurricane Ivan's observed best track is illustrated by the dashed gray line and 6-hourly position markers (white squares) and the model track by the solid black line. The background colors indicate the COAMPS-TC SWH at forecast hour 41 from the 1200 UTC 14 September 2004 72-h forecast. Wind (white) and wave (black) direction vectors are plotted (relative magnitude is not indicated). The red box shows the location of the Scanning Radar Altimeter (SRA) flight in relation to the wave buoys.

UTC 14 September 2004 72-h forecast track of Hurricane Ivan brought the cyclone directly over the 14 ADCP current profilers deployed along the outer continental shelf and upper slope of the GOM just south of the Mississippi and Alabama coasts. The ADCP data indicated that the shelf currents followed Ekman dynamics with overlapping surface and bottom layers during Ivan's approach and transitioned to a dominant surface boundary layer as the wind stress peaked with Ivan's passage (Teague et al., 2007). In addition, Hurricane Ivan generated very strong surface and subsurface currents on the shelf and slope. For example, the ADCP M1 measured currents in excess of 200 cm s^{-1} during the forced stage response, while currents on the slope at depths >50 m commonly exceeded 50 cm s^{-1}.

To compare the observed ocean-current response near the surface in the COAMPS-TC simulations, we followed Kuzmic et al. (2006) for the calculation of the magnitude of the complex correlation coefficient (CCC, Eq. (1)) and the angular displacement, or mean directional error (MDE, Eq. (2)), between the measured ADCP and NCOM model currents in the NCOM-to-SWAN coupled simulation (Kundu, 1976):

$$CCC = \frac{(u_o u_m + v_o v_m) + i(u_o v_m - u_m v_o)}{\sqrt{(u_o^2 + v_o^2)} \cdot \sqrt{(u_m^2 + v_m^2)}} \quad (1)$$

$$MDE = tan^{-1}\left[\frac{(u_o v_m - u_m v_o)}{(u_o u_m + v_o v_m)}\right] \quad (2)$$

where u and v are the east–west and north–south, observed (o) and modeled (m), demeaned velocities, and the angle brackets represent a time average. The CCC and MDE were computed for the six shallow-water ADCPs, which recorded near-surface ocean currents. Inherent in the computation, the CCC accounts for both the current speed and direction in its calculation of the correlation coefficient.

Table 1 compares the 72-h 1200 UTC 14 September forecast simulated and observed velocities at the location of the top bin

at each of the ADCP moorings M1–M6 (Fig. 1) that had a near-surface current measurement for the NCOM-to-SWAN coupled COAMPS-TC simulation (BHcpl, see Section 4.1.2). The model velocities were taken from the closest grid point to the moorings and interpolated to the depth of the observations. Since the M1–M6 ADCPs were shallow-depth moorings and recorded current velocities near the surface, these statistical results are important for validating that NCOM was producing satisfactory surface currents for inclusion in SWAN. To better gauge the accuracy of the near-surface ocean response to Hurricane Ivan predicted by COAMPS-TC, the timing of the prediction with respect to the TC location was corrected when performing comparisons between the model simulations and the observations. It is important to note that these comparisons are very sensitive to along-track timing errors and cross-track spatial errors, and the timing adjustments were done to reduce the effect of temporal errors in the location of the TC in the simulations. Since the model track was quite good, the temporal adjustment was calculated by just shifting the model time along the predicted track to better match the observed TC location. Only a small timing adjustment was needed to account for the COAMPS-TC timing error over the ADCP array.

For each shallow-water ADCP, current measurements were taken in intervals of 15 min. Within every 15-min interval, each ADCP recorded several measurements. These measurements were then averaged every 15 min and velocities recorded at that time. NCOM currents were then compared to the ADCP currents throughout the 72-h 1200 UTC 14 September forecast, which provided the best track and intensity forecast of Hurricane Ivan over the ADCP array in the coupled NCOM-to-SWAN simulation (the uncoupled simulation produced a nearly identical track).

The time-lag-adjusted CCC and MDE for the shallow ADCPs (M1–M6) compare well with the model results. Statistics for the period encompassing the forced ocean response to Hurricane Ivan indicate that mean CCC values approached or exceeded 0.8 and

Table 1
ADCP array ocean current statistical comparisons for the NCOM-to-SWAN coupled simulation (BHcpl) for the 72-h 1200 UTC 14 September forecast. The magnitude of the complex correlation coefficient (CCC), mean directional error (MDE), and current speed mean bias (MB) are computed for the top bins in each of the ADCPs M1-M6. The maximum current speed at each ADCP and from NCOM at the ADCP locations are also shown.

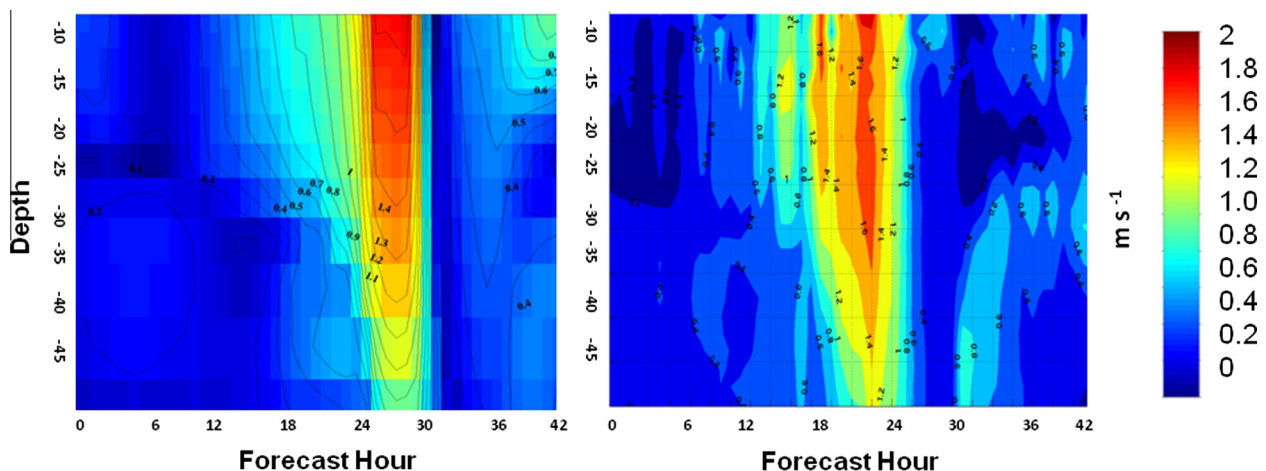| ADCP #	TOP BIN DEPTH (m)	CCC (BHcpl)	MDE (deg, BHcpl)	SPEED MB (m s^{-1})	MAX SPEED COAMPS (m s^{-1})	MAX SPEED OBS (m s^{-1})
M1	6	0.83	1.57	0.046	2.04	2.14
M2	4	0.77	8.45	0.082	1.75	1.87
M3	6	0.79	12.29	0.110	1.61	1.73
M4	10	0.78	10.44	0.121	1.77	1.96
M5	11	0.82	10.37	0.071	1.82	1.91
M6	9	0.83	15.54	0.145	1.69	1.82

Fig. 4. (a) Time series of NCOM Eulerian ocean current speed (m s^{-1}) at ADCP M1. (b) Time series of observed current speed from ADCP M1 (m s^{-1}).
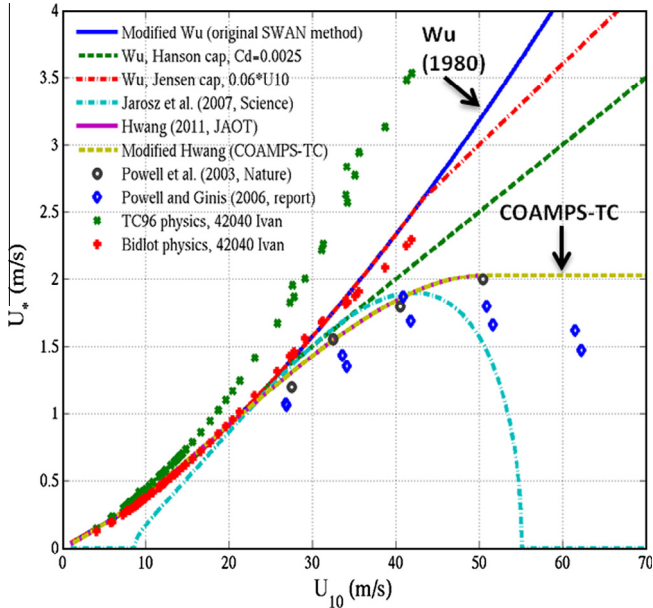
Fig. 5. The friction velocity, $u*$, as a function of 10-m wind, U_{10}, based on ocean surface drag coefficient formulations, C_{10}, from several investigators and observational data studies. Several *parametric models based on observations* are shown: default SWAN, based on Wu (1980) (blue line); Wu with drag coefficient capped at $2.5e^{-3}$ (green dashed line); Wu with drag coefficient capped at $0.06*U_{10}$ (red dot-dashed line); Jarosz et al. (2007) (cyan dashes); Hwang (2011) (magenta line); and Hwang (2011) modified as described in the text (gold dashed line). *Observational data points* shown are: Powell et al. (2003) (black circles); and Powell and Ginis (2006) (blue diamonds). Lastly, we include the friction velocities predicted by *other wave model physics* (not used herein) Tolman and Chalikov (1996, green Xs); and Bidlot et al. (2007) (also described in Ardhuin et al. (2010) (red crosses). These numerical model results are from WAVEWATCH III® (Tolman, 2009), and specifically correspond to simulations of Hurricane Ivan at the location of buoy 42040.

MDE values were 15° or less in the coupled simulation in the topmost bin for almost all of the shallow ADCPs. Additional statistics shown in Table 1 are the mean bias (MB) of the current speed between NCOM and the ADCPs as well as the maximum model and ADCP speeds for the 72-h forecast period. The results indicate that the current speed MB was generally less than 0.15 m s^{-1}, while the NCOM maximum speeds were slightly less than, but comparable to, the maximum speeds of the ADCP observations just below the surface.

Errors in the CCC and MDE for the shallow-water ADCP observations can be attributed to several factors. The model track was excellent as Ivan approached the southwestern edge of the ADCP array nearest to M11. However, from that point an almost due north model track in both simulations, which was slightly west of the observed track, continued past ADCP M11. Although simple temporal adjustments to the simulated TC location were made, this deviation in track as Ivan exited the ADCP array likely contributed to some of the MDE statistical errors. Errors in the initial conditions and the representation of the ocean current velocities at the beginning of a forecast are always critical; however, the use of 3DVAR ocean assimilation leading up to the 72-h forecast reduced this error with respect to the ADCPs. A time series of the vertical cross section of the Eulerian currents at ADCP M1 also shows a good ocean response beneath the surface as shown in Fig. 4 (not time-lag adjusted). Overall, the near-surface ocean current speed and direction response for Hurricane Ivan in COAMPS-TC was satisfactory and indicates that the NCOM surface (top-layer) currents that are being passed to SWAN were reasonable.

4.1.2. SWAN sensitivity to wave dissipation, drag coefficient, and NCOM to SWAN coupling

An evaluation of the friction velocity, $u*$, in high-wind conditions is important for the use of the new SWAN wind input and
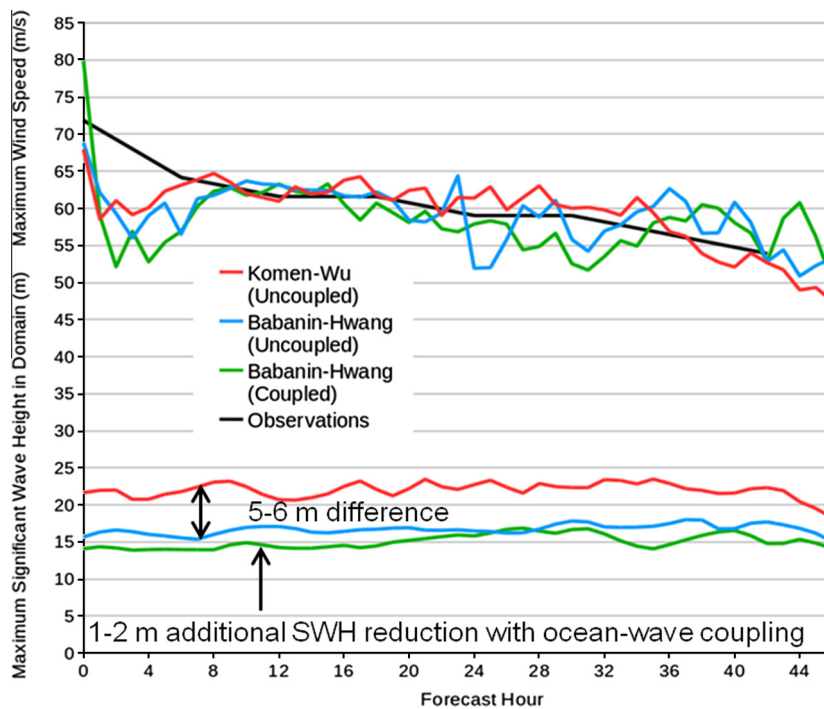

Fig. 6. Time series of maximum TC intensity and maximum SWH are illustrated for several SWAN sensitivity tests. Sensitivity tests include a combination of both Komen and Babanin wind input and dissipation parameterizations and Wu (1980) and Hwang (2011) surface ocean drag formulations. For this study, three sensitivity tests, Komen-Wu uncoupled (KWunc, red), Babanin-Hwang uncoupled (BHunc, blue), and Babanin-Hwang coupled (BHcpl, green) were completed. A portion of the 1200 UTC September 2004 72-h forecast is plotted (landfall occurs at approximately hour 40 in the simulation).

dissipation parameterizations presented by Babanin et al. (2010) (described in Appendix A) for TC simulations. The evaluation of u^* based on the 10-m wind (U_{10}) requires the specification of a 10-m ocean surface drag coefficient (C_{10}). There are many formulations of the ocean surface drag coefficient reported in the literature and Fig. 5 presents several investigators' resultant u^* formulations based on their expressions for C_{10} (e.g., Wu, 1980; Powell et al., 2003; Powell and Ginis, 2006).

Early C_{10} estimates from Wu (1980) showed u^* monotonically increasing with increasing U_{10} based on data collected from 33 experiments under neutrally-stable, open-ocean conditions. However, the value of C_{10} for high-wind conditions (greater than 30 m s^{-1}) was hypothesized since their data did not extend to such high wind speeds. In fact, SWAN utilizes the C_{10} formulation from Wu (1980) in its current version. However, since the Wu (1980) experiments, it has been observed in field measurements that C_{10} displays a saturation trend in high winds, with a possible decrease in magnitude for wind speeds greater than 40 m s^{-1}. Field studies in tropical cyclone conditions (Powell et al., 2003; Jarosz et al., 2007; Sanford et al., 2011) have shown that u^* has a tendency to asymptote to a u^* value near 2 m s^{-1} (Fig. 5) and to even decrease slightly for winds greater than 50 m s^{-1}. Hwang (2011) formulated an empirical equation to capture the saturation and decaying behavior of C_{10} in high-wind conditions based on observations from Felizardo and Melville (1995), Powell et al. (2003), and Jarosz et al. (2007):

$$C_{10} = 10^{-4}(-0.0160U_{10}^2 + 0.697U_{10} + 8.058) \qquad (3)$$

The resultant calculation for u^* based on the Hwang (2011) formulation for C_{10} is represented in Fig. 5. In this study, a modified Hwang (2011) formulation for C_{10} was tested in SWAN as well as the classic Wu (1980) formulation. Since the rapid decrease of u^* to 0 for $U_{10} > 68$ m s^{-1} in the Jarosz et al. (2007) formulation has not been verified, a modified Hwang formulation (Fig. 5, gold hatched line) was obtained by capping the value of u^* at the maximum value from Hwang (2011) formulation of about 2 m s^{-1} for $U_{10} > 50$ m s^{-1}.

The Babanin wave source terms and the modified Hwang drag coefficient formulation in SWAN were implemented in COAMPS-TC to test their effectiveness in a severe TC wind event and to investigate the sensitivity of SWAN compared to the first generation Komen et al. (1984) wave source terms and Wu (1980) drag formulation. Fig. 6 shows a comparison of the maximum SWH for Hurricane Ivan for both the old and new SWAN wave source terms and drag coefficient. Three simulations were tested: (1) Komen–Wu NCOM-SWAN uncoupled (KWunc), (2) Babanin–Hwang NCOM-SWAN uncoupled (BHunc), and (3) Babanin–Hwang NCOM-SWAN coupled (BHcpl). The maximum intensities of Hurricane Ivan for each of the aforementioned tests were very comparable, while the forecast tracks were nearly identical to the forecast track shown in Fig. 3. Upon immediate inspection, a 5–6 m difference in the maximum SWH between the KWunc and BHunc simulations was present. The implementation of the Babanin wave source terms and, more importantly, the reduced drag coefficient formulation produced a SWH result that was much more reasonable when compared to observations in high wind conditions. However, it is important to note that all the u^* formulations shown in Fig. 5 are similar for winds less than 20 m s^{-1} and will produce comparable results in SWAN at these lower wind speeds.

The further addition of NCOM-to-SWAN coupling (BHcpl) in COAMPS-TC acted primarily to reduce the maximum SWH throughout the forecast track of Hurricane Ivan by an additional 1–2 m (Fig. 6) in the presence of winds greater than 50 m s^{-1}. It is notable that the locations of maximum SWH in the BHunc and BHcpl simulations tend to be different. Comparison of the BHcpl

simulation with the KBunc simulation shows a large overall decrease in the maximum SWH of 6–8 m.

4.1.3. Comparisons to NBDC buoys

The data from several NBDC buoys were analyzed during the cyclone's passage over the eastern and central GOM for comparison with the Hurricane Ivan forecasts. NBDC buoy 42040, just offshore of the northern GOM coast and within the ADCP array (Fig. 1), was directly impacted by the inner core of Hurricane Ivan. Surface currents at the location of buoy 42040 are normally quite weak, generally less than 10 cm s^{-1}, but as the cyclone passed over the buoy, the near-surface currents exceeded 2 m s^{-1} as measured by ADCP M1 (Table 1). Fig. 7a is a plot of SWH for both the BHunc and BHcpl simulations compared to the observations at buoy 42040. An along-track time lag is evident in the plot of about 3–6 h. The
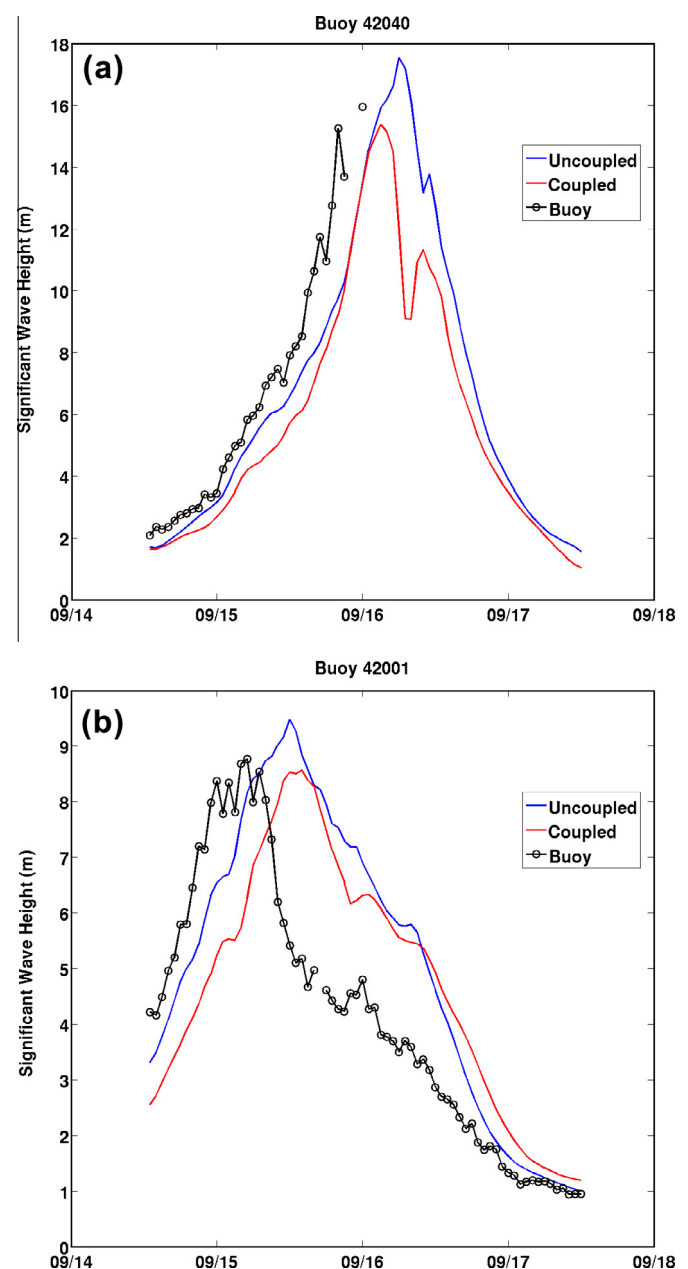

Fig. 7. Comparison of SWH from the uncoupled (blue, BHunc) and coupled (red, BHcpl) 1200 UTC 14 September 72-h forecasts with NDBC buoy observations (black). (a) Buoy 42040; (b) Buoy 42001.

BHunc simulation produced SWHs of 17–18 m at this location, while the BHcpl simulation produced maximum SWHs of 15–16 m, a difference of about 2 m. Hence, the addition of the strong, hurricane-induced surface currents from NCOM into SWAN lowered the SWHs at the location of buoy 42040 to more reasonable values. Although not shown, the SWHs in the KWunc simulation

for buoy 42040 were in excess of 18 m, with maximum heights approaching 20 m.

Comparisons with data from another NDBC buoy, 42001, located outside of Hurricane Ivan's inner core, also showed improvement when NCOM was coupled to SWAN. Surface ocean currents in September 2004 revealed a very large warm-core eddy that had shed from the Loop Current and was centered just east of buoy 42001. Pre-Ivan surface currents at buoy 42001 were on the order of 0.5 m s^{-1}. Inclusion of the surface currents from NCOM in SWAN in the BHcpl simulation reduced the predicted SWHs by about 1 m at buoy 42001 compared with the BHunc simulation (Fig. 7b). For both buoys 42040 and 42001, the effect of including strong surface currents in the SWAN calculations, whether hurricane-induced or environmental, acted to improve the SWHs in SWAN at these locations. Results from other buoys in the BHcpl simulation, which were far from the region of strongest winds and in areas of weak surface currents, showed only modest differences from the BHunc simulation.

4.1.4. Scanning radar altimeter (SRA) and satellite altimeter comparisons

Although useful in point comparisons, the array of NDBC buoys in the GOM cannot adequately capture the evolving wave field in each quadrant of a tropical cyclone. As a TC translates in a certain direction, it is unlikely that fixed buoys would provide enough information about the wave field in each quadrant relative to the TC's center. In addition, not all buoys provide directional wave spectra, which further reduce the quantification of the wave field. The SRA, on the other hand, is an aircraft instrument with high spatial and temporal resolution along the flight tracks, and it has been successfully used to observe the wave field in the vicinity of a TC (Wright et al., 2001).

For the purpose of this study, the SRA NASA aircraft flight track that best fits the simulation window began at 2008 UTC 14
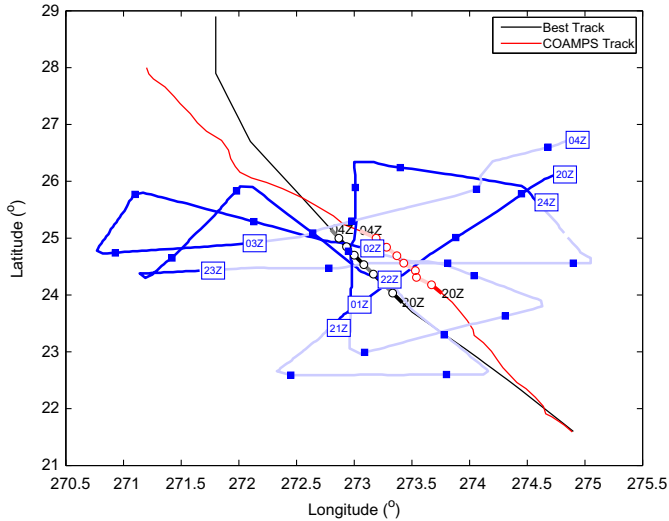

Fig. 8. Flight track of the airborne SRA (blue line) starting at 2000 UTC 14 September 2004 and ending at 0400 UTC 15 September 2004. Full hours are printed in boxes and 15 min intervals are denoted with blue squares. Flight segments starting with even (odd) hours are colored dark (light) blue. The observed (black) and simulated (red) TC tracks are shown. The circles on the two tracks represent hourly locations of the storm center.
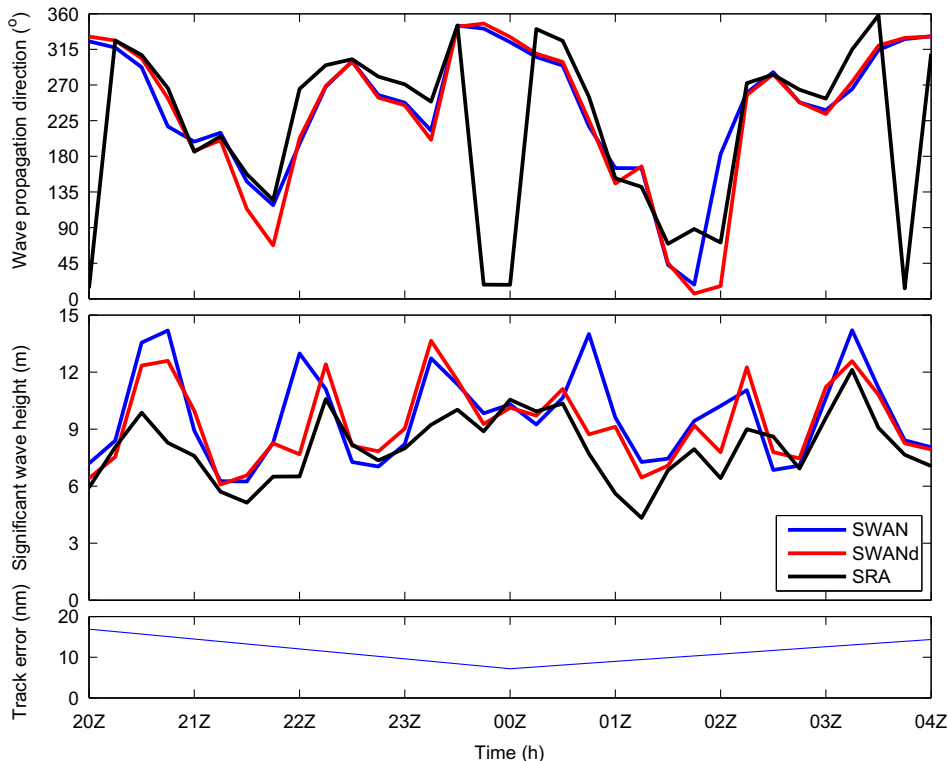

Fig. 9. Aircraft SRA (black), SWAN (blue), and track-adjusted SWAN (red) wave propagation direction (top, degrees) and SWH (middle, m) are plotted along with BHcpl track error (bottom, nautical miles (nm)) from 2000 UTC 14 September 2004 to 0400 UTC 15 September 2004.

September and completed at 0347 UTC 15 September, a flight duration of 7 h and 39 min (Fig. 8). The output fields from SWAN were interpolated to the locations of the airborne sensor along the flight track at 15-min intervals (e.g., at 2000 UTC, 2015 UTC, 2030 UTC...) for the 0000 UTC 14 September forecast. The first (last) SRA measurements at 2008 UTC (0347 UTC) were used for comparison with the SWAN data at 2000 UTC (0400 UTC). The SRA data were not regularly spaced in time, so the data chosen were those measurements closest to the regular 15-min intervals. The maximum time discrepancy was less than four minutes, except for the first and last set of measurements. The two parameters used for the validation of SWAN, the SWH and mean wave propagation direction (MWPD), were calculated from the directional spectra as follows:

$$SWH = 4\sqrt{\int\int E(\omega,\vartheta)d\omega\,d\vartheta} \qquad (4)$$

$$MWPD = tan^{-1}\left[\frac{\int\int sin\vartheta E(\omega,\vartheta)d\omega\,d\vartheta}{\int\int cos\vartheta E(\omega,\vartheta)d\omega\,d\vartheta}\right] \qquad (5)$$

where $E(\omega,\theta)$ is the variance density spectrum as a function of frequency (ω) and azimuthal angle (θ). For the SRA data, both of these parameters were readily calculated. Additionally, if the wave spectrum was bimodal, both the primary and secondary propagation directions were given.

A comparison of the SRA and SWAN SWH and MWPD for the 0000 UTC 14 September BHcpl forecast is shown in Fig. 9. The SWH mean error (ME) in the simulation is 1.62 m and the root-mean-square error (RMSE) is 2.55 m; however, if the comparisons are adjusted to take in account spatial and temporal track errors, the SWH ME is reduced to 1.25 m and the RMSE is reduced to 1.78 m. The largest differences in SWH occur primarily during the peaks of the simulated SWH. The model MWPD is fairly similar to the observed value (Fig. 9), with a ME of about −7°, and a RMSE of 34.2° when adjusted for spatial and temporal track errors. The propagation direction was captured very well; however, the SWAN waves were propagating to the left of the actual wave field (a MWPD ME of −24.71° when adjusted for track errors); therefore, they were shifted by about a quarter of a quadrant (22.5°).

In addition to the flight SRA data, several satellite altimeter measurements of winds and SWH were also compared to the model results. The three satellites, Envisat, ERS-2, and GFO, provided numerous passes that yielded useful observational information. Fig. 10a shows the ground passes made by each of the satellites for 14–16 September 2004. Notably, the position of each pass was such that no measurements were made within the inner core of Ivan. Fig. 10b shows statistics for all 806 SWH measurements taken by satellite compared with the 1200 UTC 14 September 72-h BHcpl and BHunc forecasts, which were adjusted for track error for optimal comparison. The BHcpl RMSE was 0.974 m compared
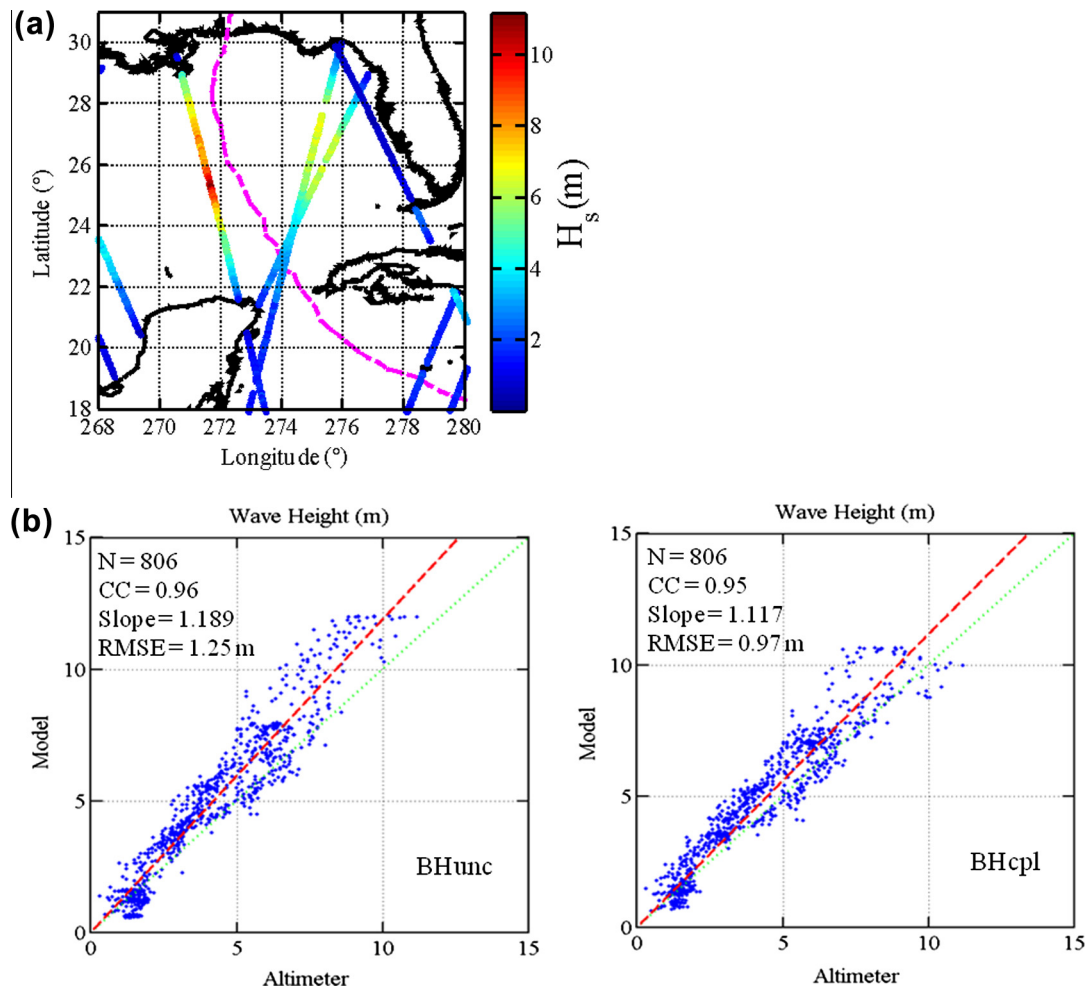

Fig. 10. (a) Satellite altimeter paths with observed SWH (H_s) for the 1200 UTC 14 September 2004 forecast. The magenta line represents the observed track of Hurricane Ivan. (b) Scatter diagrams of model versus altimeter SWH for all 806 observations for the BHunc (bottom left) and BHcpl (bottom right) simulations. The correlation coefficient (CC), the linear, least-squares fit (red dashed line), and the RMSE are shown on each plot.

to 1.250 m for BHunc, indicating a reduction in SWH in the coupled simulation. These results are consistent with the lowering of the SWH in the sensitivity tests when the ocean currents are included in the wave model coupling.

4.2. Wave-to-ocean coupling in COAMPS-TC: Stokes Drift Current

The SDC and wind stress vectors in COAMPS-TC were analyzed to determine the model's ability to resolve SDC interactions at scales of a few km near the dynamic inner core of a TC. The Stokes production of TKE during Hurricane Ivan and its effect on vertical mixing was calculated following Kantha and Clayson (2004, see Appendix B). Although there are no in situ observational data to explicitly evaluate the SDC for Hurricane Ivan, recent theory on the subject implies that the SDC is important in TC ocean–wave interactions (Sullivan et al., 2012).

Fig. 11 shows the misalignment angle between the SDC and the surface wind stress vectors at forecast hour 43 during the BHcpl simulation. Hurricane Ivan was translating to the north at about 10 kts near the ADCP array at this time. The eyewall of the hurricane is circled in Fig. 11. The misalignment angle between the SDC and the wind stress near the core of the hurricane approached 180° near point A, which is near the eyewall on the left (west) side of the track. The idealized study of Van Roekel et al. (2012) indicated that a misalignment angle greater than 90° works to inhibit mixing directly caused by Langmuir circulation and, in the most extreme case of a misalignment angle of 180°, there is minimal generation of LT. A comparison of the Stokes shear production of TKE for the BHcpl simulation at points A and B in Fig. 11 on the left and right sides of the hurricane track, respectively, is shown in Table 2. Calculation of the Stokes production term at forecast hours 38–50 indicated that at point A, the Stokes production term becomes very small at forecast hour 42 and even shows a small negative value at forecast hour 43 at the time of the greatest misalignment angle. Note that a negative contribution of the Stokes production to the total production of TKE implies that the inclusion of the SDC is acting to decrease the vertical mixing. The

Table 2
Calculations of the Stokes shear TKE production term (Eq. (8)) for the BHcpl simulation at points A and B in Fig. 11.

Forecast hour	Point A ($\times 10^{-4}$ m^2 s^{-3})	Point B ($\times 10^{-4}$ m^2 s^{-3})	Point A misalignment angle (°)	Point B misalignment angle (°)
38	7.4	7.4	14.5	9.4
39	8.5	8.2	12.1	6.0
40	9.0	7.9	10.8	5.4
41	9.0	7.6	13.4	4.8
42	1.9	7.6	61.2	0.6
43	-0.5	8.9	142.0	3.4
44	6.4	7.5	15.3	0.1
45	6.3	7.3	4.9	0.1
46	5.8	6.1	4.2	1.1
47	5.2	4.9	1.1	0.7
48	4.6	4.6	0.3	5.0
49	4.2	2.7	0.5	0.7
50	3.0	2.3	2.3	2.2

results shown in Table 2 are similar to the findings of Sullivan et al. (2012) in their LES simulations of LT during a hurricane, i.e., large misalignment angles between the wind and waves can occur on the left-hand-side of a hurricane during the passage of the eye, and the large misalignment angle can result in oppositely signed vertical gradients of the Eulerian current and the SDC, which can significantly reduce the contribution of LT to vertical mixing. Hence, the Kantha and Clayson (2004) parameterization of the enhancement of vertical mixing by LT using Stokes production terms in the TKE and TLS equations provides a behavior of LT with respect to the alignment between the wind and the waves that is consistent with recent LES studies.

The SDC can also be an important component of the total current velocity in areas with significant waves. Fig. 12 shows a time-depth plot of the SDC in the upper 15 m for forecast hours 25–50 at point A in Fig. 11, which is located near the west side of the eyewall of Hurricane Ivan at forecast hour 40. The near-surface SDC became quite large as the eyewall passed directly over
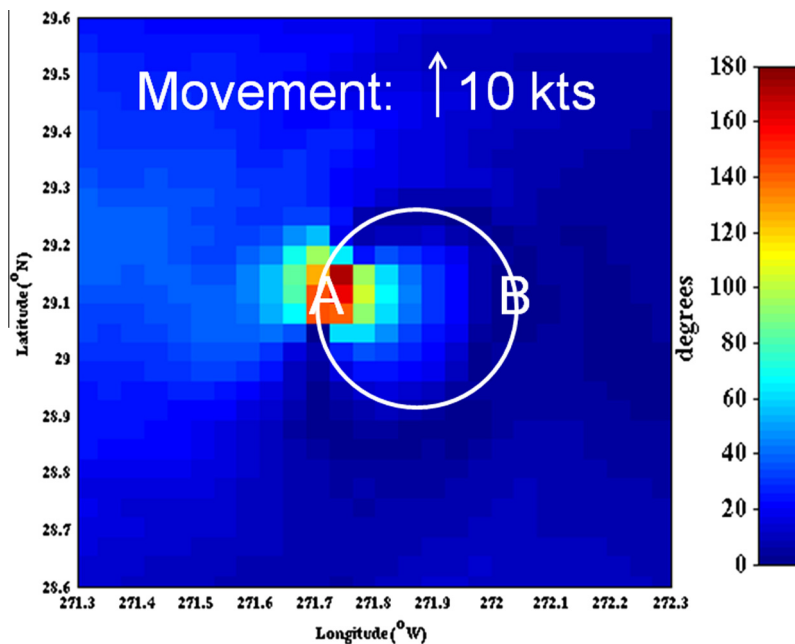

Fig. 11. Misalignment angle (degrees) between the SDC and surface wind stress vectors at forecast hour 43 in the BHcpl simulation. The Stokes shear TKE production is analyzed at points A and B. Hurricane Ivan's eyewall is denoted by the circle, and the translation direction and speed are also indicated on the plot.
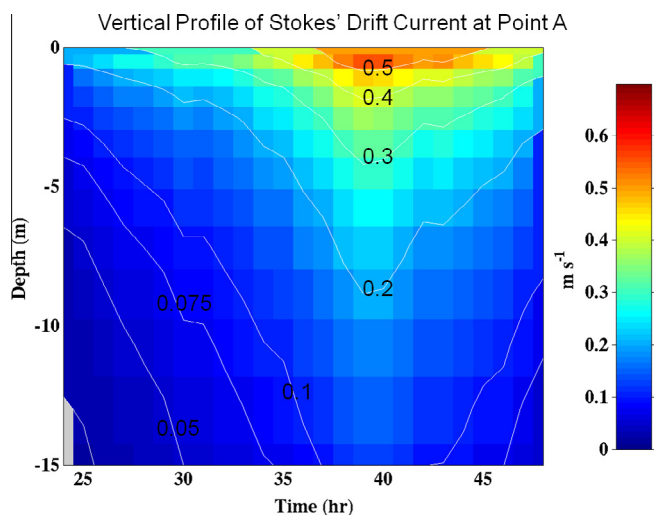
Fig. 12. Time-depth plot of SDC velocity computed from the SWAN spectra at point A in Fig. 11.

point A, i.e., near 0.5 m s^{-1}, at which time the surface winds exceeded 50 m s^{-1}. The maximum near-surface Eulerian currents, as discussed in Section 3.1.1 and shown in Table 1, are approximately 2 m s^{-1}, indicating that the SDC may be as large as 10–25% of the Eulerian current near the surface in extreme TC conditions.

5. Summary

The COAMPS-TC model simulations for Hurricane Ivan showcased the state-of-the-art ESMF coupling of three independent models: the COAMPS atmospheric model, NCOM, and SWAN. The unique and comprehensive observational data set for Hurricane Ivan allowed for the evaluation of model performance based on recent improvements to the atmospheric, oceanic, and wave physics, while gaining a general but improved understanding of the primary effects of ocean–wave model coupling in high-wind conditions. The new wind input and dissipation source terms (Babanin et al., 2010; Rogers et al., 2012) and wave drag coefficient formulation (Hwang, 2011), based on field observations, significantly improved SWAN's wave forecasts for the simulations of Hurricane Ivan conducted in this study. In addition, the passing of ocean current information from NCOM to SWAN further improved the TC wave field.

Future work with COAMPS-TC will continue to focus on the air-ocean-wave parameterizations to improve TC track and intensity. Recent advances, shown here in COAMPS-TC, include the addition of a wave component, SWAN (Booij et al., 1999), to exchange wave-related properties such as the Stokes' Drift Current (SDC), wave-radiation stress gradients, and the near-bottom wave motions that affect bottom drag in shallow water. Although a generalized and simplified SDC and TKE study is shown here for Hurricane Ivan, additional work is needed to better understand the effects of wave-to-ocean model coupling on the upper ocean in high wind TC conditions. Additionally, an examination of wave-to-atmosphere model feedback and different NCOM ocean mixing schemes is currently ongoing. Recent data obtained during the Impact of Typhoons on the Ocean in the Pacific (ITOP) study provide excellent ocean vertical temperature profiles for several TCs to evaluate SDC-induced turbulence in NCOM. Planned efforts will also include evaluation of the WW3 model, which has recently been coupled with COAMPS-TC to provide an alternative wave model. This research is a continuation of an Office of Naval Research (ONR) sponsored National Oceanographic Partnership Program (NOPP) project

with the Rosenstiel School of Marine and Atmospheric Science (RSMAS) at the University of Miami and the University of Rhode Island to generate a unified, coupled model interface for providing a common feedback mechanism between different TC models, such as the Hurricane Weather Research and Forecast (HWRF) System model. The overall ocean-to-wave model coupling results within COAMPS-TC for Hurricane Ivan are encouraging and provide a platform for continued research into the next generation of air–ocean–wave coupled models.

Appendix A. SWAN deepwater source functions discussion

The observation-based wind input and whitecapping source terms of Rogers et al. (2012) are used in the SWAN simulations presented in this study. These formulations (referred to as the "Babanin" parameterizations in this paper) are based on earlier work by Donelan et al. (2006), Babanin and Young (2005), Young and Babanin (2006), Tsagareli (2009), Tsagareli et al. (2010), and Babanin et al. (2010). The wind input source terms in the new parameterization were taken directly from the observational work of Donelan et al. (2006) in high wind conditions over Lake George, Australia, and modified to scale with the friction velocity u^*. The new dissipation function is observation-consistent insofar as it conforms to two features of dissipation in the real ocean as reported in the literature during the past decade. The first feature has a two-phase dissipation, with waves of any particular frequency dissipating either due to (1) the instability (and breaking) of waves of that frequency or (2) the destabilization by larger breaking waves (e.g., through turbulence). The second feature establishes a wave-breaking threshold, such that when the local spectral density falls below a spectral threshold, no breaking occurs at that frequency. These two features were not included together in any numerical model until very recently (by Tsagareli, 2009 in an academic model and by Ardhuin et al., 2010 in WW3). Both features contrast sharply with the dissipation terms of the previous generation (e.g., Komen et al., 1984; WAMDI Group, 1988; Booij et al., 1999), in which all waves were considered breaking at all times and every wave system affected the strength of dissipation of all other systems in a physically implausible manner (Rogers et al., 2003). The third major source function in deep water is that for four-wave nonlinear interaction. For this term, we use the Discrete Interaction Approximation (Hasselmann et al., 1985), as is customary for operational wave models of this type (WAMDI 1988; Tolman, 2009; Booij et al., 2009).

Appendix B. Parameterization of vertical mixing by Langmuir circulation/turbulence

Kantha and Clayson (2004, KC04) parameterize the enhancement of vertical mixing by Langmuir circulation and Langmuir

turbulence in the MYL2.5 turbulence model by adding Stokes shear-production terms to the TKE and TLS equations. These terms consist of the product of the vertical turbulent momentum flux of the Eulerian current times the vertical shear of the SDC and have the form

$$TKE_{SDC} = -\rho \overline{u'w'} \frac{\partial U_s}{\partial z} - \rho \overline{v'w'} \frac{\partial V_s}{\partial z} \qquad (6)$$

where $\overline{u'w'}$ and $\overline{v'w'}$ are the vertical turbulent momentum fluxes, u', v', and w' are the turbulent velocity fluctuations, U_s and V_s are the horizontal components of the SDC, and z is the vertical coordinate. Note that this form for the Stokes production terms in the TKE equation is fairly well established (e.g., McWilliams et al., 1997; Sullivan et al., 2007; Grant and Belcher, 2009; Janssen, 2012; Sullivan et al., 2012) and can be derived (in analogous fashion to the derivation of the standard Eulerian shear-production terms in the TKE equation) from Reynolds averaging of the vortex-force and Bernoulli-head terms in the kinetic energy equations formed from the momentum equations used to explicitly simulate Langmuir circulation (McWilliams et al., 1997).

In the MYL2.5 turbulence model, the vertical turbulent momentum fluxes are computed from the vertical shear of the Eulerian current

$$\overline{u'w'} = -K_m \frac{\partial U}{\partial z} \quad \overline{v'w'} = -K_m \frac{\partial V}{\partial z} \qquad (7)$$

where K_m is the vertical turbulent mixing coefficient for momentum computed by the MYL2.5 turbulence model and U and V are the horizontal components of the Eulerian velocity. Substituting (7) into (6), the Stokes production of TKE is calculated as

$$TKE_{SDC} = K_m \left(\frac{\partial U}{\partial z} \frac{\partial U_s}{\partial z} + \frac{\partial V}{\partial z} \frac{\partial V_s}{\partial z} \right) \qquad (8)$$

KC04 include the Stokes production terms (8) in both the TKE and TLS equations. In the TLS equation, KC04 scale the Stokes production terms with a higher weighting than the standard Eulerian shear-production terms, i.e., the Stokes production terms are scaled by a factor of 7.2, whereas the Eulerian shear-production terms are scaled by a factor of 1.8. Note that in the KC04 paper, the value used to scale the Stokes production terms in the TLS equation is given as 4, which is incorrect (Lakshmi Kantha, personal communication).

The effect of the KC04 parameterization is that the presence of the SDC tends to increase the vertical mixing coefficients by increasing both the TKE and the TLS. Note, however, that if the vertical shear of the Eulerian current and the vertical shear of the SDC are of different sign, the Stokes TKE production terms can make a negative contribution to the production of TKE. Hence, the Stokes production terms are sensitive to the relative alignment of the wind-driven, near-surface, Eulerian current and the SDC, i.e., to the relative alignment of the wind and the waves.

References

Ardhuin, F., Rogers, E., Babanin, A., Filipot, J.-F., Magne, R., Roland, A., van der Westhuysen, A., Queffeulou, P., Lefevre, J.-M., Aouf, L., Collard, F., 2010. Semi-empirical dissipation source functions for ocean waves. Part I: Definitions, calibration and validations. J. Phys. Oceanogr. 40, 1917–1941.

Babanin, A.V., Young, I.R., 2005. Two-phase behaviour of the spectral dissipation of wind waves. In: Proc. Fifth Int. Symp. Ocean Waves Measurement and Analysis, Madrid, Spain, ASCE, p. 51.

Babanin, A., Chalikov, D., Young, I., Savelyev, I., 2007. Predicting the breaking onset of surface water waves. Geophys. Res. Lett. 34, L07605.

Babanin, A.V., Tsagareli, K.N., Young, I.R., Walker, D.J., 2010. Numerical investigation of spectral evolution of wind waves. Part II: Dissipation term and evolution tests. J. Phys. Oceanogr. 40, 667–683.

Barron, C.N., Kara, A.B., Hurlburt, H.E., Rowley, C., Smedstad, L.F., 2004. Sea surface height predictions from the global Navy Coastal Ocean Model (NCOM) during 1998–2001. J. Atmos. Ocean. Tech. 21 (12), 1876–1894.

Bennis, A.-C., Ardhuin, F., Dumas, F., 2011. On the coupling of wave and three-dimensional circulation models: choice of theoretical framework, practical implementation, and adiabatic tests. Ocean Modell. 40, 260–272.

Bidlot, J.-R., Janssen, P., Abdalla, S., 2007. A revised formulation of ocean wave dissipation and its model impact. ECMWF Tech. Rep. Memo. 509, Reading, United Kingdom, 27 pp.

Booij, N., Ris, R.C., Holthuijsen, L.H., 1999. A third-generation wave model for coastal regions. Part I: Model description and validation. J. Geophys. Res. 104 (C4), 7649–7666.

Booij, N., Haagsma, I.J.G., Holthuijsen, L.H., Kieftenburg, A.T.M.M., Ris, R.C., van der Westhuysen, A.J., Zijlemam, 2009. SWAN cycle III version 40.72AB User Manual, Delft University.

Campbell, T., Allard, R., Preller, R., Smedstad, L., Wallcraft, A., Chen, S., Hao, J., Gaberšek, S., Hodur, R., Reich, J., Fry, C.D., Eccles, V., Cheng, H.-P., Cheng, J.-R.C., Hunter, R., DeLuca, C., Theurich, G., 2010. Integrated modeling of the battlespace environment. Comput. Sci. Eng. 12 (5), 36–45.

Carnes, M.R., Fox, D., Rhodes, R., 1996. Data assimilation in a north Pacific ocean monitoring and prediction system. J. Geophys. Res. 95 (C10), 17979–17992.

Chen, S., Campbell, T.J., Jin, H., Gaberšek, S., Hodur, R.M., Martin, P.J., 2010. Effect of two-way air–sea coupling in high and low wind speed regimes. Mon. Weather Rev. 138, 3579–3602.

Cummings, J.A., 2005. Operational multivariate ocean data assimilation. Q. J. R. Met. Soc. 131, 3583–3604.

Daley, R., Barker, E., 2001. NAVDAS: formulation and diagnostics. Mon. Weather Rev. 129, 869–883.

Davies, A.M., Lawrence, J., 1994. Examining the influence of wind and wind-wave turbulence on tidal currents using a three-dimensional hydrodynamic model including wave–current interaction. J. Phys. Oceanogr. 24, 2441–2460.

Donelan, M.A., Babanin, A.V., Young, I.R., Banner, M.L., 2006. Wave follower measurements of the wind input spectral function. Part 2. Parameterization of the wind input. J. Phys. Ocean. 36 (8), 1672–1688.

Donelan, M.A., Curcic, M., Chen, S.S., Magnusson, A.K., 2012. Modeling waves and wind stress. J. Geophys. Res. 117, C00J23.

Doyle, J.D., 2002. Coupled atmosphere–ocean wave simulations under high wind conditions. Mon. Weather Rev. 130, 3087–3099, http://dx.doi.org/10.1175/1520-0493(2002)130<3087:CAOWSU>2.0.CO;2.

Doyle J., Jin, Y., Hodur, R.M., Chen, S., Jin, H., Moskaitis, J., Reinecke, A., Black, P., Cummings, J., Hendricks, E., Holt, T., Liou, C.-S., Peng, M., Reynolds, C., Sashegyi, K., Schmidt, J., Wang S., 2012. Real-Time Tropical Cyclone Prediction Using COAMPS-TC. Adv. Geosci. Taipei Review Volumes (in press).

Drennan, W.M., Graber, G.C., Hauser, D., Quentin, C., 2003. On the wave age dependence of wind stress over pure wind seas. J. Geophys. Res. 108 (C3), 8062.

Fan, Y., Ginis, I., Hara, T., 2009a. The effect of wind–wave–current interaction on air–sea momentum fluxes and ocean response in tropical cyclones. J. Phys. Oceanogr. 39, 1019–1034.

Fan, Y., Ginis, I., Hara, T., Wright, C.W., Walsh, E.J., 2009b. Numerical simulations and observations of surface wave fields under an extreme tropical cyclone. J. Phys. Oceanogr. 39, 2097–2116.

Felizardo, F.C., Melville, W.K., 1995. Correlations between ambient noise and the ocean surface wave field. J. Phys. Oceanogr. 25, 513–532.

Ginis, I., Dikinov, K.Z., Khain, A.P., 1989. A three dimensional model of the atmosphere and the ocean in the zone of a typhoon. Dikl. Akad. Nauk SSSR 307, 333–337.

Grant, A.L.M., Belcher, S.E., 2009. Characteristics of Langmuir turbulence in the ocean mixed layer. J. Phys. Oceanogr. 39, 1871–1887.

Halliwell Jr, G.R., Shay, L.K., Brewster, J.K., Teague, W.J., 2011. Evaluation and sensitivity of an ocean model response to Hurricane Ivan. Mon. Weather Rev. 139, 921–945.

Hanley, K.E., Belcher, S.E., Sullivan, P.P., 2010. A global climatology of wind–wave interaction. J. Phys. Oceanogr. 39 (8), 1871–1887. http://dx.doi.org/10.1175/2009JPO4119.1.

Hanley, K., Belcher, S., Sullivan, P., 2011. J. Phys. Oceanogr. 41, 1814–1817. http://dx.doi.org/10.1175/JPO-D-11-051.1, Reply.

Hara, T., Belcher, S.E., 2004. Wind profile and drag coefficient over mature ocean surface wave spectra. J. Phys. Oceanogr. 34, 2345–2358.

Hasselmann, S., Hasselmann, K., Allender, J.H., Barnett, T.P., 1985. Computations and parameterizations of the nonlinear energy transfer in a gravity-wave spectrum. Part II: Parameterizations of the nonlinear energy transfer for application in wave models. J. Phys. Oceanogr. 15, 1378–1391.

Hwang, P.A., 2011. A note on the ocean surface roughness spectrum. J. Atmos. Ocean. Tech. 28, 436–443.

Jacob, S.D., Shay, L.K., Mariano, A.J., Black, P.G., 2000. The 3D oceanic mixed layer response to Hurricane Gilbert. J. Phys. Oceanogr. 30, 1407–1429.

Janssen, P.A.E.M., Viterbo, P., 1996. Ocean waves and the atmospheric climate. J. Clim. 9, 1269–1287.

Janssen, P.A.E.M., Bidlot, J., Hansen, B., 2000. Diagnosis of the ECMWF ocean–wave forecasting system. ECMWF Technical Memorandum, p. 318.

Janssen, P.A.E.M., Doyle, J.D., Bidlot, J., Hansen, B., Isaksen, L., Viterbo, P., 2002. Impact and feedback of ocean waves on the atmosphere. In: Perrie, W. (Ed.), Advances in Fluid Mechanics 33, Atmosphere–Ocean Interactions, vol. I. WIT Press.

Janssen, P.A.E.M., 2012. Ocean wave effects on the daily cycle in SST. J. Geophys. Res. 117, C00J32. http://dx.doi.org/10.1029/2012JC007943.

Jarosz, E., Mitchell, D.A., Wang, D.W., Teague, W.J., 2007. Bottom-up determination of air–sea momentum exchange under a major tropical cyclone. Science 315, 1707–1709.

Knaff, J.A., DeMaria, M., Sampson, C.R., Peak, J.E., Cummings, J., Schubert, W.H., 2013. Upper oceanic energy response to tropical cyclone passage. J. Climate 26, 2631–2650.

Kantha, L.H., Clayson, C.A., 2004. On the effect of surface gravity waves on mixing in the oceanic mixed layer. Ocean Modell. 6, 101–124.

Komen, G.J., Hasselmann, S., Hasselmann, K., 1984. On the existence of a fully developed wind–sea spectrum. J. Phys. Oceanogr. 14, 1271–1285.

Kundu, P.K., 1976. Ekman veering observed near the ocean bottom. J. Phys. Oceanogr. 6, 238–242.

Kuzmic, M., Janekovic, I., Book, J.W., Martin, P.J., Doyle, J.D., 2006. Modeling the northern Adriatic double-gyre response to intense bora wind: A revisit. J. Geophys. Res. 111, C03S13.

Liou, C.-S., Sashegyi, K.D., 2011. On the initialization of tropical cyclones with a three-dimensional variational analysis. Nat. Hazards. http://dx.doi.org/10.1007/s11069-011-9838-0.

McWilliams, J.C., Sullivan, P.P., Moeng, C.-H., 1997. Langmuir turbulence in the ocean. J. Fluid Mech. 334, 1–30.

Mitchell, D.A., Teague, W.J., Jarosz, E., Wang, D.W., 2005. Observed currents over the outer continental shelf during Hurricane Ivan. Geophys. Res. Lett. 32, L11610.

Moon, I.-J., Hara, T., Ginis, I., 2004a. Effect of surface waves on air–sea momentum exchange. Part I: Effect of mature and growing seas. J. Atmos. Sci. 61, 2321–2333.

Moon, I.-J., Ginis, I., Hara, T., 2004b. Effect of surface waves on air–sea momentum exchange. Part II: Behavior of drag coefficient under tropical cyclones. J. Atmos. Sci. 61, 2334–2348.

Morey, S.L., Bourassa, M.A., Dukhovskoy, D.S., O'Brien, J.J., 2006. Modeling studies of the upper ocean response to a tropical cyclone. Ocean Dyn. 56, 594–606.

Perkins, H.T., de Strobel, F., Gualdisi, L., 2000. The barney sentinel trawl-resistant ADCP bottom mount: design, testing, and application. IEEE J. Ocean. Eng. 25, 430–436.

Powell, M.D., Vickery, P.J., Reinhold, T.A., 2003. Reduced drag coefficient for high wind speeds in tropical cyclones. Nature 422, 279–283.

Powell, M.D., Ginis, I., 2006. Drag coefficient distribution and wind speed dependence in tropical cyclones. NOAA HRD-AOML report. 5 pp.

Price, J.F., 1981. Upper ocean response to a hurricane. J. Phys. Oceanogr. 11, 153–175.

Rogers, W.E., Hwang, P.A., Wang, D.W., 2003. Investigation of wave growth and decay in the SWAN model: three regional-scale applications. J. Phys. Oceanogr. 33, 366–389.

Rogers, W.E., Babanin, A.V., Wang, D.W., 2012. Observation-consistent input and whitecapping-dissipation in a model for wind-generated surface waves: description and simple calculations. J. Atmos. Ocean. Tech. 29 (9), 1329–1346.

Rosmond, T.E., Teixeira, J., Peng, M., Hogan, T.F., Pauley, R., 2002. Navy operational global atmospheric prediction system (NOGAPS): forcing for ocean models. Oceanography 15, 99–108.

Sanford, T.B., Price, J.F., Girton, J.B., 2011. Upper-ocean response to Hurricane Frances (2004) observed by profiling EM-APEX floats. J. Phys. Oceanogr. 41, 1041–1056.

Shay, L.K., Elsberry, R.L., Black, P.G., 1989. Vertical structure of the ocean current response to hurricanes. J. Phys. Oceanogr. 19, 649–669.

Signell, R.P., Beardsley, R.C., Graber, H.C., Capotondi, A., 1990. Effect of wave–current interaction on wind-driven circulation in narrow, shallow embayments. J. Geophys. Res. 95 (C6), 9671–9678.

Smith, S.R. Cummings, J. A., Spence, P., Carroll, S.N., Rowley, C., Smedstad, O.M., Chu, P., Lunde, B., Shriver, J., Helber, R. 2011. Validation Test Report for the Navy Coupled Ocean Data Assimilation 3D Variational Analysis (NCODA-VAR) System, Version 3.43. NRL Memorandum Report NRL/MR/7320-11-9363. Naval Research Laboratory, Stennis Space Center, MS.

Snaith, H., Busswell, G., Sheera, H., Collard, F., Piollé, J., Queffeulou, P., Quilfen, Y., Ash, E., Cotton, D., Carter, D., Poulter, D., Williams, I., 2010. GLOBWAVE: A new generation of satellite wave products. In: Proceedings of OceanObs'09: Sustained Ocean Observations and Information for Society. Venice, Italy, 21–25 September 2009. ESA Publication.

Sullivan, P.P., McWilliams, J.C., Melville, W.K., 2007. Surface gravity wave effects in the oceanic boundary layer: large-eddy simulation with vortex force and stochastic breakers. J. Fluid Mech. 593, 405–452.

Sullivan, P., Romero, L., McWilliams, J.C., Melville, J.K., 2012. Transient evolution of Langmuir turbulence in ocean boundary layers driven by hurricane winds and waves. J. Phys. Oceanogr. 42, 1959–1980.

Teague, W.J., Jarosz, E., Carnes, M.R., Mitchell, D.A., Hogan, P.J., 2006. Low-frequency current variability observed at the shelfbreak in the northeastern Gulf of Mexico: May–October 2004. Cont. Shelf Res. 26, 2559–2582.

Teague, W.J., Jarosz, E., Wang, D.W., Mitchell, D.A., 2007. Observed oceanic response over the upper continental slope and outer shelf during Hurricane Ivan. J. Phys. Oceanogr. 37, 2181–2206.

Tolman, H.L., Chalikov, D., 1996. Source terms in a third-generation wind–wave model. J. Phys. Oceanogr 26, 2497–2518.

Tolman, H.L, 2009. User manual and system documentation of WAVEWATCH III™ version 3.14, Tech. Note, NOAA/NWS/NCEP/MMAB, 220 pp.

Tsagareli, K.N., 2009. Numerical investigation of wind input and spectral dissipation in evolution of wind waves. Ph.D. Thesis, The University of Adelaide, South Australia, p. 219.

Tsagareli, K.N., Babanin, A.V., Walker, D.J., Young, I.R., 2010. Numerical investigation of spectral evolution of wind waves. Part 1: Wind input source function. J. Phys. Oceanogr. 40 (4), 656–666.

Van Roekel, L.P., Fox-Kemper, B., Sullivan, P.P., Hamlington, P.E., Haney, S.R., 2012. The form and orientation of Langmuir cells for misaligned winds and waves. J. Geophys. Res. 117, C05001. http://dx.doi.org/10.1029/2011JC007516.

WAMDI Group, 1988. The WAM model – a third generation ocean wave prediction model. J. Phys. Oceanogr. 18, 1775–1810.

Wang, D.W., Mitchell, D.A., Teague, W.J., Jarosz, E., Hulbert, M.S., 2005. Extreme waves under Hurricane Ivan. Science 309 (5736), 896.

Warner, J.C., Sherwood, C.R., Signell, R.P., Harris, C., Arango, H.G., 2008. Development of a three-dimensional, regional, coupled wave, current, and sediment-transport model. Comput. Geosci. 34, 1284–1306.

Warner, J.C., Armstrong, B., He, R., Zambon, J.B., 2010. Development of a coupled ocean–atmosphere–wave-sediment transport (COAWST) modeling system. Ocean Modell. 35, 230–244.

Wright, C.W., Walsh, E.J., Vandemark, D., Krabill, W.B., Garcia, A.W., Houston, S.H., Powell, M.D., Black, P.G., Marks, F.D., 2001. Hurricane directional wave spectrum spatial variation in the open ocean. J. Phys. Oceanogr. 31, 2472–2488.

Wu, J., 1980. Wind-stress coefficients over sea surfaces near neutral conditions: a revisit. J. Phys. Oceanogr. 10, 727–740.

Young, I.R., Babanin, A.V., 2006. Spectral distribution of energy dissipation of wind-generated waves due to dominant wave breaking. J. Phys. Oceanogr. 36 (3), 376–394.

Young, I.R., Banner, M.L., Donelan, M.A., Babanin, A.V., Melville, W.K., Veron, F., McCormick, C., 2005. An integrated system for the study of wind wave source terms in finite depth water. J. Atmos. Ocean. Tech. 22 (7), 814–828.